Supplementary information for

Synergistic Effect of Zn-N Coordination Inducing Enhanced Hydrophobicity and Dipole Activation for Efficient Photocatalytic ROS Evolution

Xiaojuan Bai*[a,b], Jiaqian Dong[b] and Wenzhi Zhang[b]

[a] Key Laboratory of Urban Stormwater System and Water Environment, Ministry of Education, Beijing University of Civil Engineering and Architecture.

[b]Beijing Energy Conservation & Sustainable Urban and Rural Development Provincial and Ministry Co-construction Collaboration Innovation Center, Beijing University of Civil Engineering and Architecture, Beijing, China. Beijing 100044, China. E-mail: baixiaojuan@bucea.edu.cn

E-mail: baixiaojuan@bucea.edu.cn (Xiaojuan Bai)

Experimental procedures

Supplementary Text 1. Materials

2,4-diamino-6-phenyl-1,3,5-triazine (DAT, 1.1395g, 1mol), 3,3′,4,4′-Biphenyltetracarboxylic dianhydride (BPDA, 1.4684, 1mol), zinc acetate dihydrate ($Zn(oAc)_2$), sodium bicarbonate ($NaHCO_3$, 99%), methanol (MeOH, 99%), formic acid (FA, 99%), N, N-Dimethylformamide (DMF, 99%), sodium hydroxide (NaOH), hydrochloric acid (HCI), potassium iodide (KI), potassium phthalate monobasic (KHP), sodium sulfate (Na_2SO_4), potassium carbonate (**(**K_2CO_3), potassium chloride **(**KCl), L-histidine (L-his), p-benzoquinone (p-BQ), silver nitrate ($AgNO_3$), tert-butanol (TBA), disodium ethylenediaminetetraacetate (EDTA-2Na), potassium nitrate (KNO_3), and antibiotic pollutants (sulfamethoxazole SMX, sulfanilamide SA and Sulfadiazine SD), humic acid (HA), naphthalene (NAP), tetracycline (TC), and sodium diclofenac (DCF) , deionized water. All purchased reagents were of analytical grade or above and could be used without further purification.

Supplementary Text 2. Synthesis of TIC and HTIC

TIC Weight accurately 1.1395 g of 2,4-diamino-6-phenyl-1,3,5-triazine (DAT) and 1.4684 g of 3,3′,4,4′-Biphenyltetracarboxylic dianhydride (BPDA). These reagents were transferred to an agate mortar and ground manually until uniform. The mixture was then placed into a labeled crucible with a lid and heated in a muffle furnace to 325 °C, with a heating rate of 7 °C/min, and maintained at this temperature for 4 hours. The resulting solid was ground again to a fine consistency, washed with alcohol, and subsequently dried. The obtained yellow powder was designated as TIC.

HTIC Selected sodium bicarbonate as the gas sacrificial agent and zinc acetate as the precursor for the micro- to nano-structured framework to achieve hydrophobic interface modulation. Weight accurately 1.1395 g of 2,4-diamino-6-phenyl-1,3,5-triazine (DAT), 1.4684 g of 3,3′,4,4′-Biphenyltetracarboxylic dianhydride (BPDA), the preparations contained 10%, 20%, and 30% (w/w) sodium bicarbonate and zinc acetate, respectively. These reagents were transferred to an agate mortar and ground manually until uniform. The mixture was then placed into a labeled crucible with a lid and heated in a muffle furnace to 325 °C, with a heating rate of 7 °C/min, and maintained at this temperature for 4 hours. The resulting solid was ground again to a fine consistency, washed with alcohol, and subsequently dried. The obtained brown powder was designated as HTIC.

Supplementary Text 3. Characterization of photocatalysts

Scanning electron microscopy (SEM) and energy dispersive spectroscopy (EDS) were used to

analyze the appearance of the sample using an SU−8010 scanning electron microscope. Transmission electron microscopy (TEM) images were taken by HT7700 transmission electron microscopy. The surface roughness was examined by Cypher VRS atomic force microscopy (AFM). Fourier transform infrared (FT-IR) spectra of the TIC and HTIC were obtained by the VERTEX 70 spectrophotometer. The X-ray diffraction (XRD) pattern of the powder under Cu Kα radiation was recorded using a Japanese Rigaku Smart Lab SE. The X-ray photoelectron spectroscopy (XPS) analysis was performed using ESCALAB Xi+ (Thermo Fisher Scientific, USA). Electron paramagnetic resonance (EPR) energy spectra were measured at room temperature using an ESR 300E (Bruker, Germany) spectrometer. On a JNM-ECZ600R solid-state nuclear magnetic resonance spectrometer, the ^{13} C cross-polarized magic angle spinning (CP-MAS) solid-state nuclear magnetic resonance (NMR) spectra were recorded with a 3.2-mm magic angle spinning probe. The Bruner-Emmett-Teller (BET) specific surface area was measured using a BSD-660MA6M instrument at 77 K using N_2 adsorption and desorption isotherms. The Temperature-Programmed Desorption (O_2-TPD) was measure to evaluate the O_2 adsorption characteristics by a BSD-Chem C200 instrument at 300 °C. The Hall effect measurement was conducted using an Ecopia HMS-7000 Hall effect measurement system to determine the carrier concentration of TIC and HTIC. In situ infrared spectroscopy (In situ FT-IR) was used to analyze intermediates in the photocatalytic process, using VERTEX 80v (Bruker, Germany). The Zeta potentials were analyzed by the Zeta sizer 26 Nano ZS90 (Malvern, UK).

The ultraviolet−visible diffuse reflectance spectra (UV-vis DRS) were recorded for the dry-pressed disk samples using a UV3600PLUS spectrophotometer (Shimadzu, Japan) with $BaSO_4$ as a reference. The optical bandgap (Eg) was calculated according to the following equation:

$$(\alpha \cdot h\vartheta)^{1/n} = B(h\vartheta - E_g)$$

Where α is the adsorption coefficient, h is the Planck constant, ν is the light frequency, B is a constant and Eg is the corresponding bandgap. In addition, the n factor is determined by the nature of the electron transition. Particularly, n = 1/2 means a direct bandgap transition, and n = 2 suggests an indirect bandgap transition.

Thermogravimetric (TGA) analysis was performed using Rigaku TG/DTA 8122 to assess stability. The glass transition temperature (Tg) was determined by differential scanning calorimetry

(DSC) using HITACHI DSC200. Molecular weight of HTIC was measured by Gel Permeation Chromatography (GPC) using an Agilent 1260 Infinity II GPC/SEC system, two PL-MIXED-C columns (7.5 × 50 mm, 5 μm; 7.5 × 300 mm, 5 μm) were connected in series, the mobile phase was spectral DMF (> 99.9 %, containing 0.1 % lithium bromide)； the apparent molecular weights were determined on a PL-MIXED-C columns using linear polystyrene standards. The intermediate products generated during degradation were analyzed by Liquid Chromatography-Mass Spectrometry (LC-MS).

The efficiency of the degradation of the SMX was measured by Acquity UPLC H−Class (Waters, America). The mobile phases of SMX consisted of MeOH and 0.1% formic acid solution (40 : 60, v/v) with a flow rate of 0.2 ml/min and were used with a UV detector.

Supplementary Text 4. Photocatalytic production of hydrogen H_2O_2

5 mg of photocatalyst was dispersed in 25 mL of aqueous solution. Subsequently, the dispersion was sonicated for 5 min with continuous stirring for 30 min. All photocatalytic reactions were carried out in an air atmosphere under the irradiation of a 300W xenon lamp. 1.5 mL of the solution was removed every 10 min and the solution was filtered through a 0.45 μm filter into a centrifuge tube. The amount of H_2O_2 was analyzed by iodometry 0.5 mL of 0.1 mol/L potassium hydrogen phthalate ($C_8H_5KO_4$) aqueous solution and 0.5 mL of 0.4 mol/L potassium iodide (KI) aqueous solution were added to the obtained solution, which was then kept for 30 min. The H_2O_2 molecules reacted with iodide anions (I^{-1}) under acidic conditions ($H_2O_2 + 3I^- + 2H^+ \rightarrow I_3^- + 2H_2O$) to produce triiodide anions.

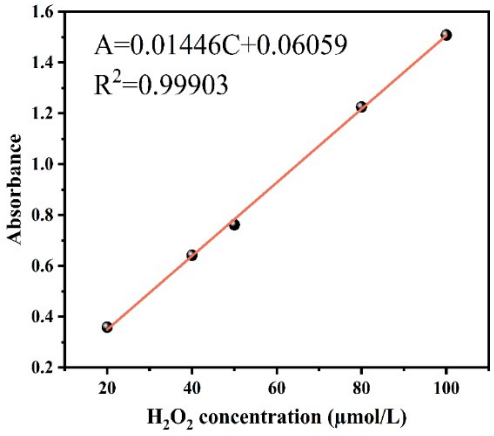

The empirical graph depicting the correlation between concentration of H_2O_2 and absorbance.

Supplementary Text 5. Apparent quantum yields (AQY) and solar-to-chemical energy

conversion (SCC)

The optical power intensity corresponding to monochromatic light was measured using an optical power meter (PL-MW2000, Beijing Porphyry Technology) under the irradiation of a xenon lamp light source (PL-SXE300D, Beijing Porphyry Technology) using different band-pass filters (380 nm, 420 nm, 450 nm, 500 nm, and 550 nm). The formula for the calculation of the AQY is as follows:

$$\mathrm{AQY}(\%) = \frac{2 \times (\text{number of produced } H_2O_2 \text{ molecules})}{\text{number of incident photons}} \times 100\%$$

$$\text{number of produced } H_2O_2 \text{ molecules} = C_{H_2O_2} \times N_A$$

Incident photon number:

$$N_{incident} = \frac{Pt}{h\nu} = \frac{Pt\lambda}{hc} = \frac{ISt\lambda}{hc}$$

Where $N_A = 6.022\times10^{23}$ units/mol; I is the optical power intensity (W m^{-2}); S is the irradiated area (11.34 cm^2 in this work); t is the reaction time (s); λ is the wavelength length of monochromatic light (m); h is Planck's constant (6.626×10^{-34} m^2 kg s^{-1}); and c is the speed of light in free space (3.0×10^8 m s^{-1}). (Units: 1 W = 1 J/s, 1 J = 1 kg m^2/s^2).

The AQY% value of HTIC at different wavelengths:

λ=380nm AQY=

$$\frac{2 \times 6.022 \times 1023 \times 16.53 \times 10 - 6 \times 6.626 \times 10 - 34 \times 3 \times 108}{26.2 \times 11.34 \times 10 - 4 \times 3600 \times 380 \times 10 - 9} \times 100\% = 9.74\%$$

λ=420nm AQY=

$$\frac{2 \times 6.022 \times 1023 \times 35 \times 10 - 6 \times 6.626 \times 10 - 34 \times 3 \times 108}{59.1 \times 11.34 \times 10 - 4 \times 3600 \times 420 \times 10 - 9} \times 100\% = 8.29\%$$

λ=450nm AQY=

$$\frac{2 \times 6.022 \times 1023 \times 32.5 \times 10 - 6 \times 6.626 \times 10 - 34 \times 3 \times 108}{86.7 \times 11.34 \times 10 - 4 \times 3600 \times 450 \times 10 - 9} \times 100\% = 4.9\%$$

λ=500nm AQY=

$$\frac{2 \times 6.022 \times 1023 \times 31.5 \times 10 - 6 \times 6.626 \times 10 - 34 \times 3 \times 108}{108.4 \times 11.34 \times 10 - 4 \times 3600 \times 500 \times 10 - 9} \times 100\% = 3.41\%$$

λ=550nm AQY=

$$\frac{2 \times 6.022 \times 1023 \times 17.09 \times 10 - 6 \times 6.626 \times 10 - 34 \times 3 \times 108}{142.4 \times 11.34 \times 10 - 4 \times 3600 \times 550 \times 10 - 9} \times 100\% = 1.28\%$$

The solar-to-chemical energy con version (SCC) efficiency was determined by using an AM 1.5G solar simulator as the light source (1000 W·m^{-2}). 5 mg of catalyst and 25 ml of pure water

were used for the SCC test without continuous O_2 input during the photocatalytic test.

$$\text{SCC efficiency}(\%) = \frac{\Delta G(H_2O_2 \times n(H_2O_2)}{t_{ir} \times S_{ir} \times I_{AM}} \times 100\%$$

In the equation, $\triangle G(H_2O_2) = 117\ kJ \cdot mol^{-1}$, is the free energy for H_2O_2 generation. $n(H_2O_2)$ is the amount of H_2O_2 generated during the photocatalytic reaction. The irradiation time t_{ir} is 3600s, and the irradiated sample area (S_{ir}) is $11.34 \times 10^{-4}\ m^2$. I_{AM}, the total irradiation intensity of the AM 1.5 global spectra (300nm - 2500nm), is $1000\ W \cdot m^{-2}$.

The SCC (%) of HTIC:

$$\text{SCC efficiency (\%)} = \frac{117 \times 103 \times 495.47 \times 10 - 6}{3600 \times 11.34 \times 10 - 4 \times 1000} \times 100\% = 1.42\%$$

Supplementary Text 6. Photocatalytic degradation of antibiotics

In the Photocatalytic degradation experiment, 5 mg of the catalyst was added to 25 mL of 5 ppm antibiotics (Sulfamethoxazole (SMX), Sulfonamide (SA) and Sulfadiazine (SD)) and ultrasonically dispersed for 15 min in the dark. Before irradiation, the mixture was stirred in the dark for 30 min to reach the adsorption-desorption equilibrium. 1.5 mL of solution was taken out at stated intervals and centrifuged to remove the catalyst. The degradation efficiency of the antibiotics was measured by Acquity UPLC H-Class (Waters, America).

The mobile phases of SMX consisted of MeOH and 0.1% formic acid solution (60 : 40, v/v) with a flow rate of 0.2 mL/min and were used with a UV detector operating at 278 nm. The mobile phase of SA and SD consisted of methanol and 0.1% formic acid solution (60 : 40, v/v) at a flow rate of 0.2 mL/min using a UV detector with a wavelength of 270 nm. The quasi-primary kinetic analysis was calculated according to the following equation:

$$-\ln[C/C_0] = kt$$

Supplementary Text 7. Experimental water sample

Lake water from the campus of Beijing University of Civil Engineering and Architecture (BUCEA). The simulated water was formulated to reflect the pollutant concentrations found in real water samples, in accordance with the pollutant limits stipulated in China's "Groundwater Quality Standard " (GB/T 14848-2017) and "Environmental Quality Standards for Surface Water" (GB 3838-2002). The concentrations of added inorganic anions were adjusted based on the limits

specified in these standards.

Supplementary Text 8. Electrochemical measurements

The transient photocurrent response experiments were conducted on a CHI660E electrochemical system in a three-electrode system. The sample-coated Indium tin oxide (ITO) glass, Pt wire electrode, and calomel electrode were used as the working electrode, counter electrode, and reference electrode, respectively. 0.1 M Na_2SO_4 solution was utilized as the electrolyte.

Supplementary Text 9 The radical trapping experiment

5 mg of photocatalyst was dispersed in 25 mL of aqueous solution. Subsequently, the dispersion was sonicated for 5 min with continuous stirring for 30 min. All photocatalytic reactions were carried out in an air atmosphere under the irradiation of a 300W xenon lamp. 1.5 mL of the solution was removed every 10 min and the solution was filtered through a 0.45 μm filter into a centrifuge tube. The L-histidine (L-his), disodium EDTA (EDTA-2Na), silver nitrate ($AgNO_3$), p-benzoquinone (p-BQ) and tert-butanol (TBA) were employed as scavengers for singlet oxygen ($^1O_2$), hole (h^+), electron (e^-), superoxide radical ($\cdot O_2^-$) and hydroxyl radical (·OH), respectively.

Supplementary Text 10. Rotating disk electrode (RDE) measurements

A glassy carbon rotating disk electrode (PINE Research Instrumentation, USA) served as the substrate for the working electrode, and an Ag/AgCl electrode and a Pt wire electrode as the reference and counter electrode, respectively. The working electrode was prepared as follows: HTIC (5 mg) was dispersed in EtOH (2 mL) containing Nafion (50 μL) by ultrasonication. The slurry (20 μL) was put onto the disk electrode and dried at room temperature. The linear sweep voltammograms (LSV) were obtained in an O_2-saturated 0.1 M phosphate buffer solution (pH = 7) at room temperature with a scan rate of 10 mV s^{-1} and different rotation speeds after O_2 bubbling for 10 min. During the reaction, a light source from the Xe-lamp vertically illuminated the rotating electrode, where the photoelectrochemical kinetic information and the formation of peroxide could be obtained. The average number of electrons (n) was calculated by the Koutecky-Levich equation:

$$\frac{1}{J} = \frac{1}{J_L} + \frac{1}{J_K} = \frac{1}{B\omega^{1/2}} + \frac{1}{J_K}$$

$$B = 0.62nFv^{-\frac{1}{6}}CD^{\frac{2}{3}}$$

$$n = \frac{B}{0.62F\nu^{-\frac{1}{6}}CD^{\frac{2}{3}}} = \frac{0.31}{0.62 \times 96485 \times 0.01^{-\frac{1}{6}} \times 1.26 \times 10^{-3} \times (2.7 \times 10^{-5})^{\frac{2}{3}}} = 2.19$$

Where J is the current density, J_K and J_L are the kinetic and diffusion-limiting current densities, ω is the rotating speed (rpm), F is the Faraday constant (96485 C mol^{-1}), ν is the kinetic viscosity of water (0.01 cm^2 s^{-1}), C is the bulk concentration of O_2 in water (1.26×10^{-3} $mol\cdot cm^{-3}$), and D is the diffusion coefficient of O_2 (2.7×10^{-5} cm^2 s^{-1}), respectively.

Supplementary Text 11. In situ FT-IR spectroscopy

In situ FT-IR measurements were conducted using the Bruker INVENIO R FT-IR spectrometer equipped with an in situ diffuse reflectance cell (Harrick). The light snource was a 300w xenon lamp light source without a filter. The experiments were carried out under air continuous and H_2O vapor flow conditions. The vapor and sample were blown into the reactor in the dark and kept for 30 min to reach O_2 adsorption equilibrium. A baseline was obtained before the sample started adsorption. Tests were performed every 10 min after the light was turned on for a total of 30 min.

Supplementary Text 12. Computational Details

All calculations were carried out with the Gaussian software. The B3LYP functional[1] was adopted for all calculations in combination with the D3BJ dispersion correction.[2] For geometry optimization, the def2svp basis set was used.[3] The wave function analysis and visualization are performed by Multiwfn[4] and VMD,[5] respectively.

Supplementary Figures

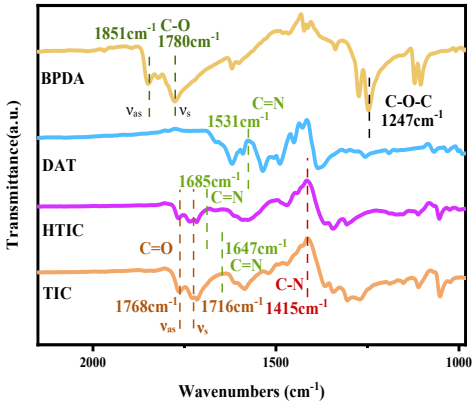

Figure S1. FT-IR spectrum of TIC and HTIC.

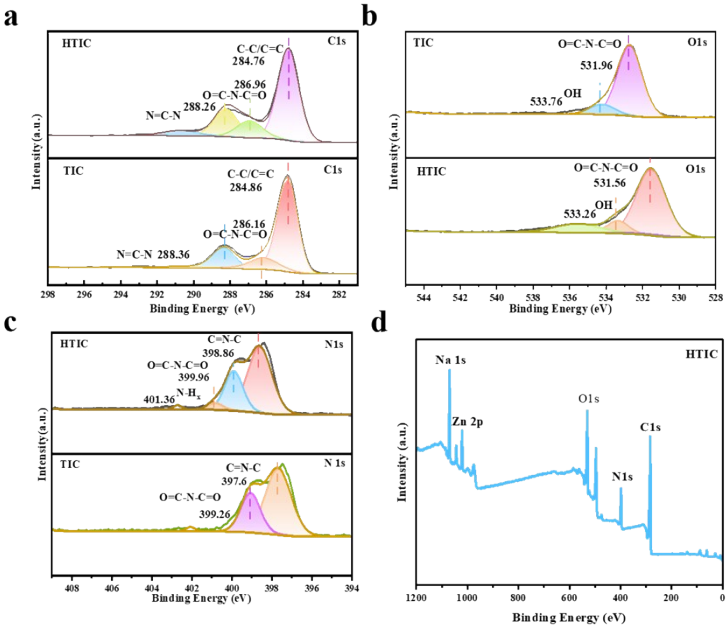

Figure S2. (a) C 1s (b) O 1s. (c) N 1s (d) XPS spectra of HTIC.

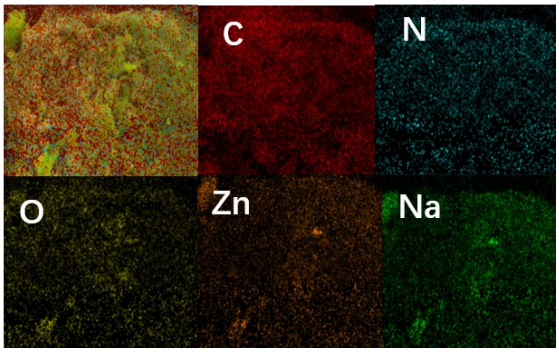

Figure S3. EDS mapping of HTIC.

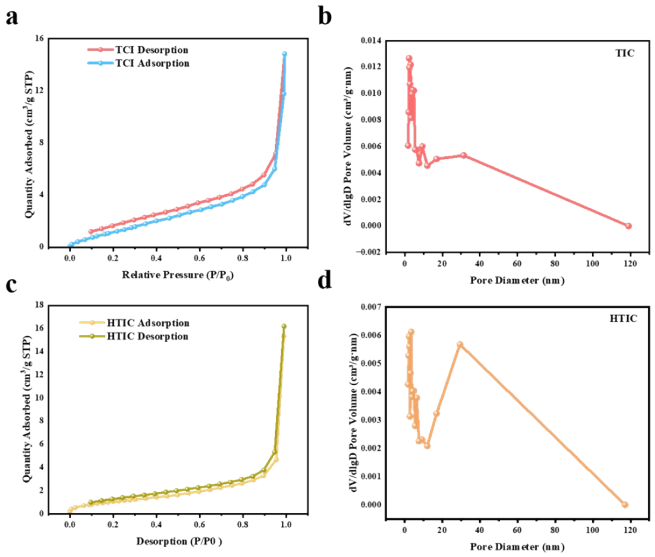

Figure S4. The BET of TIC and HTIC.

Table S1 The Pore volume and Pore size of TIC and HTIC

Sampe	Pore volume	Pore size
TIC	0.0193 cm^3/g	11.8251 nm
HTIC	0.0227 cm^3/g	23.7460 nm

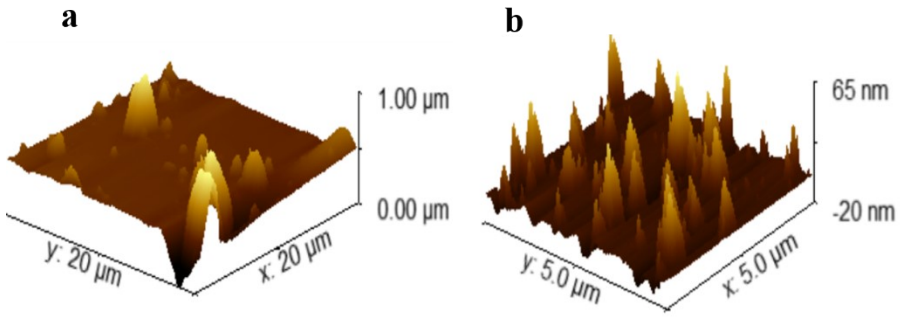

Figure S5. The AFM of TIC and HTIC.

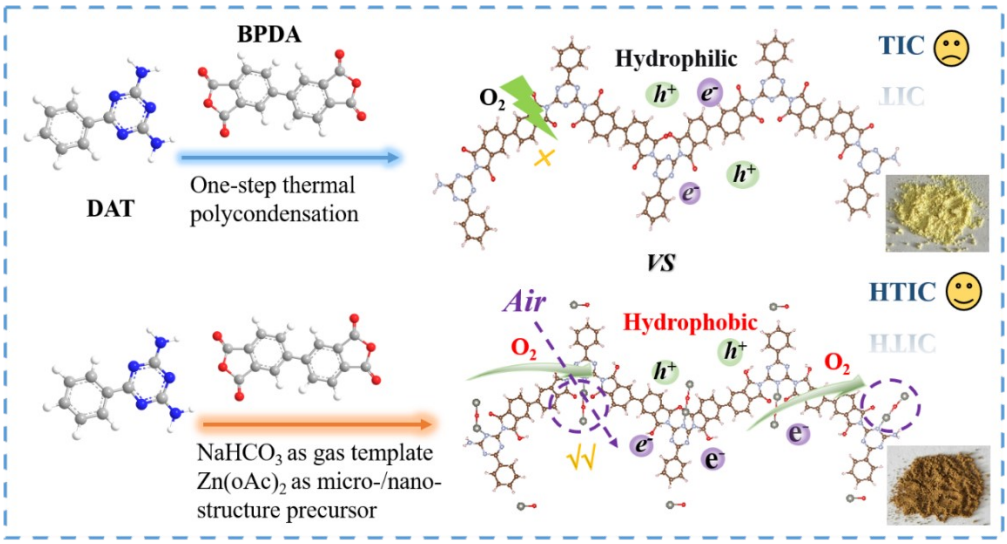

Figure S6. Synthesis and structure of TIC and HTIC.

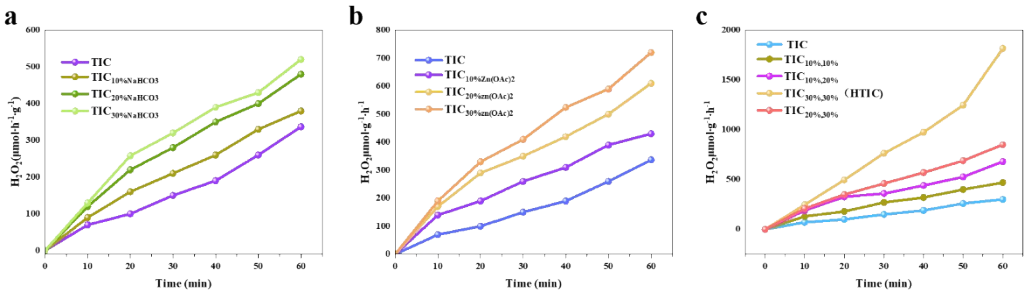

Figure S7. The production of H_2O_2 via Photocatalysis using different proportions.

Table S2. The O_2-TPD test Results of TIC and HTIC.

Sample	Heating rate	Target temperature	Total peak area
TIC	10℃/min	300℃	0.8499
HTIC	10℃/min	300℃	10.8845

Table S3. Controlled experiments for the synthesis of TIC and HTIC.

Sample	DAT（g）	BPDA（g）	$NaHCO_3$	$Zn(AOc)_2$	Synthesis Method	CA (°)
TIC	1.1395	1.4684	/	/	325℃; 4h	**82.37°**
1	1.1395	1.4684	10% (0.2608g)	/	325℃; 4h	83.96°
2	1.1395	1.4684	20% (0.5218g)	/	325℃; 4h	85.19°
3	1.1395	1.4684	30% (0.7815g)	/	325℃; 4h	85.94°
4	1.1395	1.4684	/	10% (0.2608g)	325℃; 4h	84.31°
5	1.1395	1.4684	/	20% (0.5218g)	325℃; 4h	87.69°
6	1.1395	1.4684	/	30% (0.7815g)	325℃; 4h	90.45°
7	1.1395	1.4684	10%	10%	325℃; 4h	88.39°
8	1.1395	1.4684	10%	20%	325℃; 4h	96.16°
9	1.1395	1.4684	20%	30%	325℃; 4h	106.01°
HTIC	1.1395	1.4684	30%	30%	325℃; 4h	**115.28° >90°**

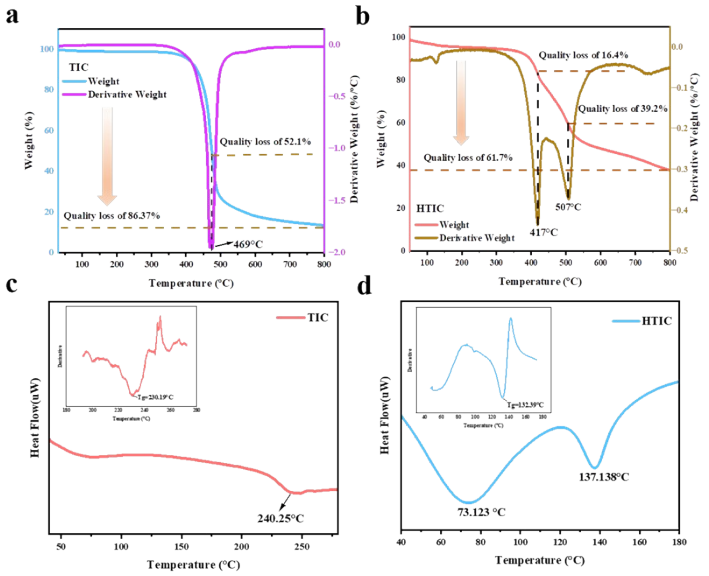

Figure S8. The TGA of (a) TIC and (b) HTIC. The DSC of (c) TIC and (d) HTIC.

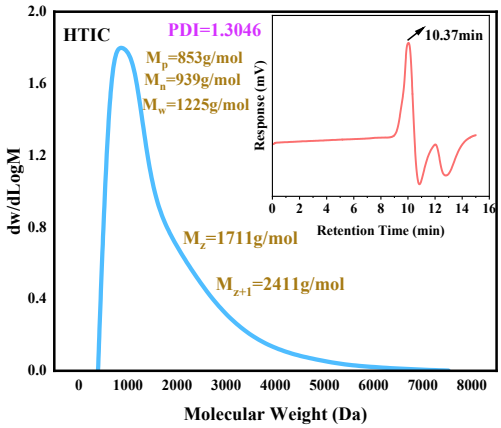

Figure S9. The GPC curves of HTIC.

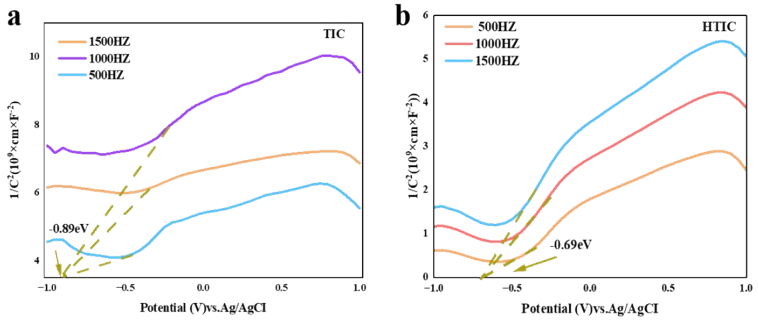

Figure S10. The Mott-Schottky curves of (a) TIC and (b) HTIC.

Table S4. The Hall-Effect Measurement Results of TIC and HTIC.

Sample	Test temperature	Resistivity	Carrier Mobility	Carrier Density	Hall Coefficient	f-factor
Unit	K	ρ (Ω·cm)	μ(cm²/V·s)	n/ (cm⁻³)	cm³/C	dimensionless
TIC	300	1.64E+10	0.27	1.42E+09	- 4.38E+09	0.98
HTIC	300	7.99E+08	0.32	2.46E+10	- 2.54E+08	0.96

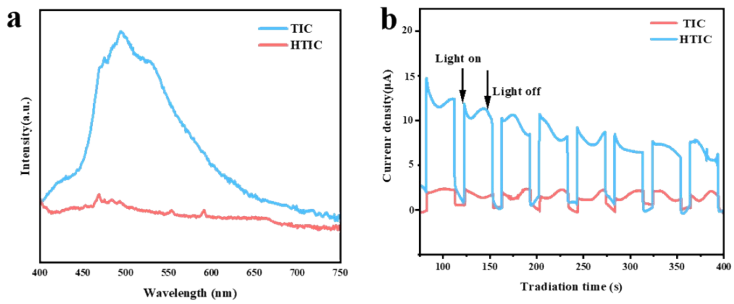

Figure S11. (a) The PL of TIC and HTIC. (b) The transient photocurrent responses of TIC and HTIC.

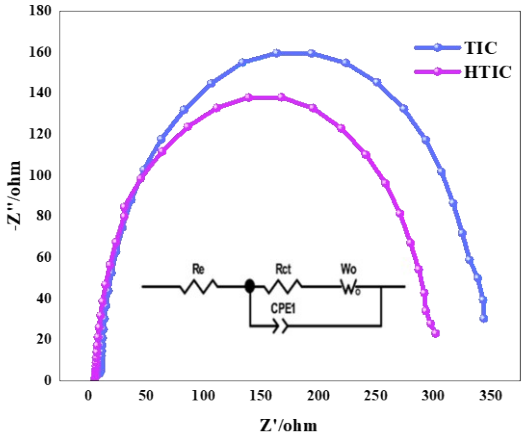

Figure S12. EIS spectra of TIC and HTIC.

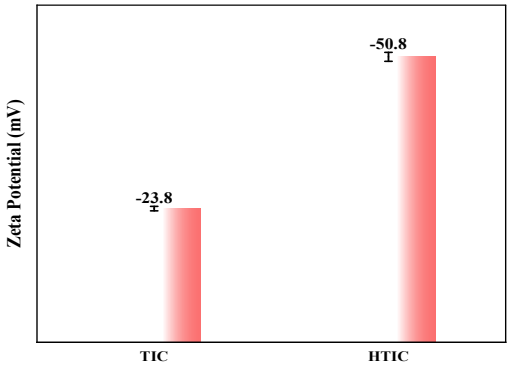

Figure S13. Zeta potential of TIC and HTIC.

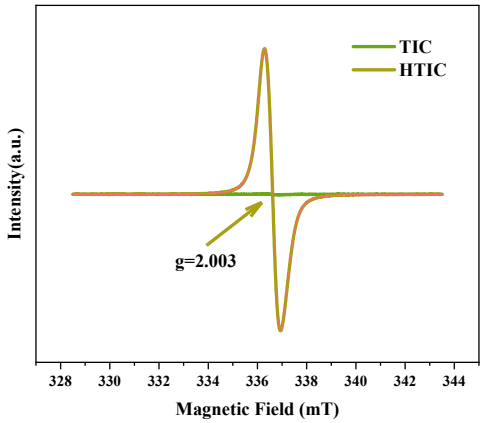

Figure S14. ESR spectra of oxygen vacancies of HTIC.

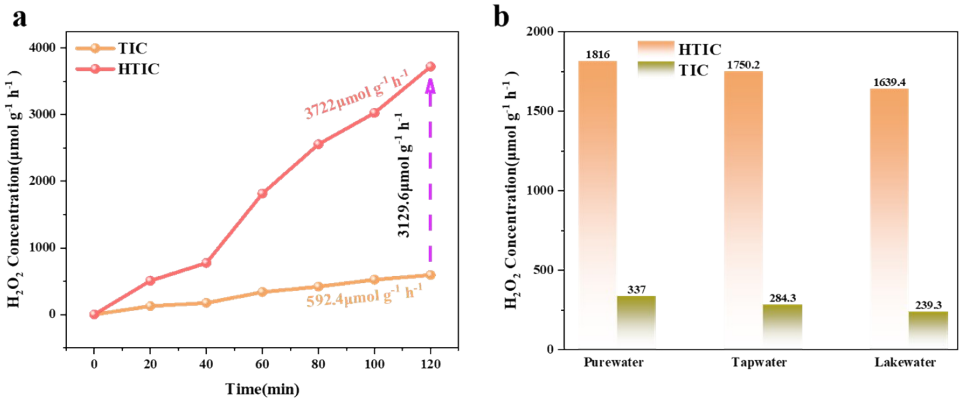

Figure S15. (a) The yield of H_2O_2 after 2 hours of photocatalytic reaction. (b)Photocatalytic H_2O_2 production in Different water bodies by TIC and HTIC.

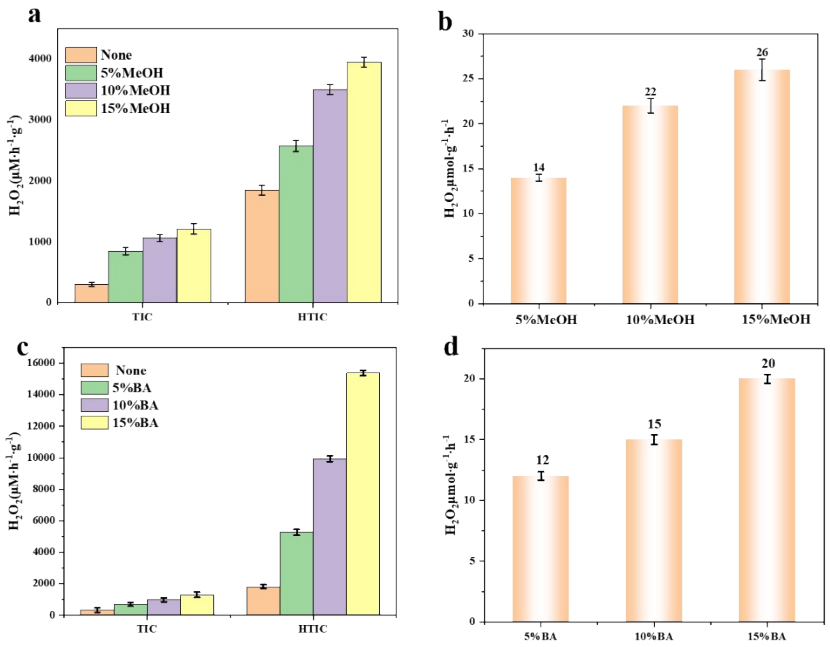

Figure S16. (a) Production of H_2O_2 by TIC and HTIC with the addition of different amounts of methanol as sacrificial agent. (b) Production of H_2O_2 under light illumination with methanol alone. (c) Production of H_2O_2 by TIC and HTIC with the addition of different amounts of benzyl alcohol as sacrificial agent. (d) Production of H_2O_2 under light illumination with benzyl alcohol alone.

Table S5. Comparison of H_2O_2 production performance of photocatalysts.

Photocatalyst	H_2O_2 yield	Catalyst dosage (mg)	AQY	SCC	Ref.
HTIC	**2667 μmol g^{-1} h^{-1}**	**5**	**9.47% at 380nm**	**1.42% AM 1.5G，λ＞420nm**	**This work**
TDB-COF（D-A）	231 μmol L^{-1} h^{-1}	5	1.4% at 365nm	-	6
Bpt-CTF	32.681μmol h^{-1}	10	8.6% at 400nm	0.2% AM 1.5G	7
CTF-BTT	5757 μmol L^{-1} h^{-1}	5	7.61% at 420nm	0.66% AM 1.5G，λ＞420nm	8
COF-2CN	1601 μmol g^{-1} h^{-1}	12.5	6.8% at 459nm	0.6% AM 1.5G	9
TZ-COF	268 μmol g^{-1} h^{-1}	15	0.6% at 475nm	0.036% AM 1.5G	10
TAPT-DHA	1629 μmol g^{-1} h^{-1}	5	7.79% at 450nm	-	11
TBD-COF	380 μmol g^{-1} h^{-1}	1	5.67% at 420nm	1.04% AM 1.5G	12
CTTP	1850 μmol g^{-1} h^{-1}	20	1.08% at 420nm	-	13
NI-TPA-NI-SO_3H	2690 μmol g^{-1} h^{-1}	5	2.27% at 400nm	0.11%AM 1.5 G	14
CHF-DPDA	1725μmol g-1 h-1	2	λ>420 nm（O_2）	-	15
sonoCOF-F2	1244μmol g-1 h-1	0.6	λ>420 nm（O_2）	AM 1.5G	16
SA-TCPP	1146.7μmol g-1 h-1	1.5 mg	λ>420 nm（O_2）	-	17
Por-HQ-COF	1525μmol g^{-1} h^{-1}	5	5.05% at 420nm	-	18

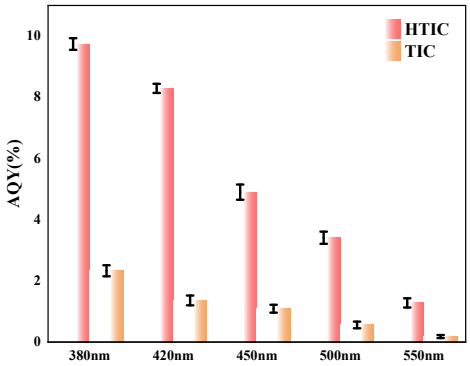

Figure S17. The AQY of TIC and HTIC.

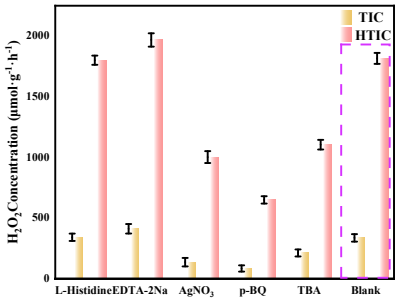

Figure S18. The yield of H_2O_2 under different sacrificial agents.

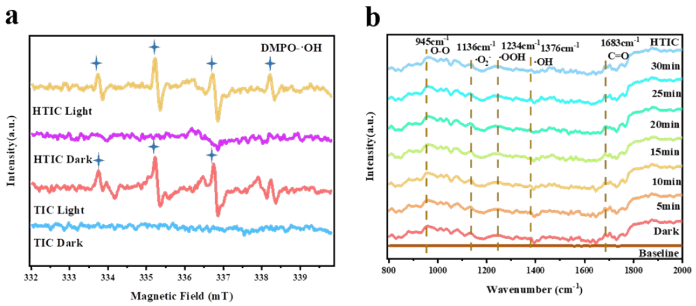

Figure S19 (a) EPR spectra of ·OH. (b) The in-situ FT-IR spectrum of HTIC.

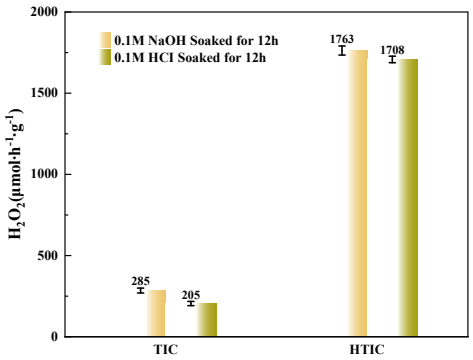

Figure S20. Photocatalytic yield of H_2O_2 after soaking in hydrochloric acid and alkali for 12 hours by TIC and HTIC.

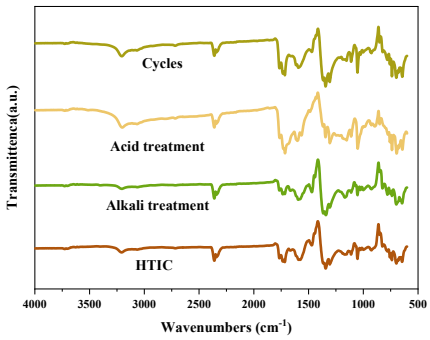

Figure S21. The FTIR spectra of HTIC after acid-base soaking and five-cycle degradation.

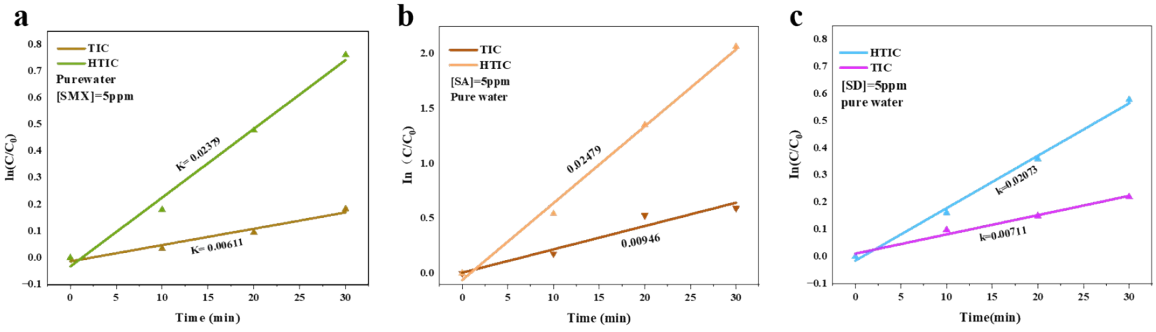

Figure S22. First-order degradation rate constant for photocatalysis.

Table S6. Water Quality Indexes of Lake water.

Sample name	pH	Index concentration (mg/L)					
		COD	TN	TP	TOC	NH_4^+-N	Electrical conductivity (μS/cm)
Lake water (Before degradation)	6.19	17.62	0.79	0.015	3.98	0.361	919.12
Lake water (After degradation)	7.5	15.24	0.65	0.010	2.28	0.241	909.73

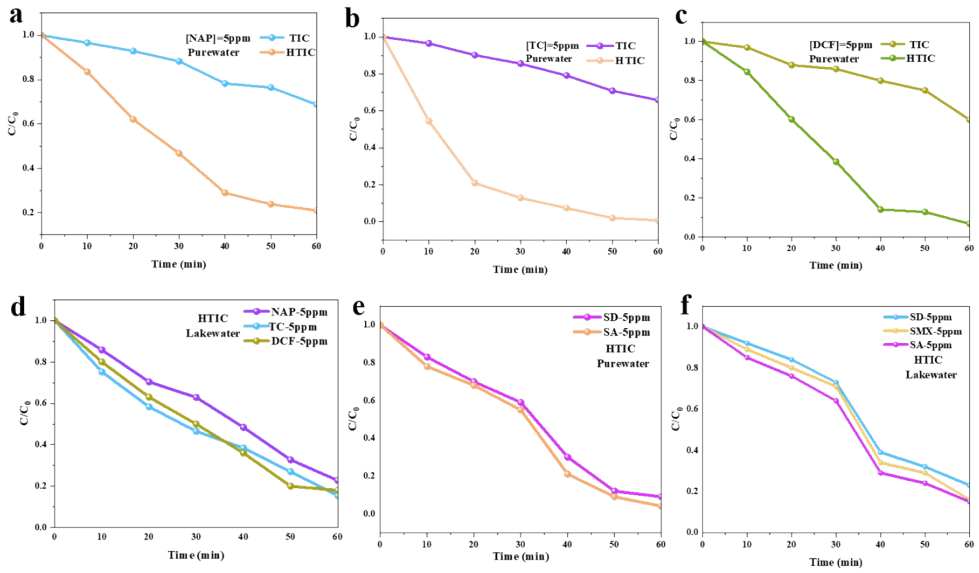

Figure S23. The photocatalytic degradation curves of different pollutants in pure water by TIC and HTIC: (a) NAP; (b) TC; and (c) DCF. (d) The photocatalytic degradation curves of NAP, TC and DCF by HTIC in lake water. (e) Degradation SA and SD in pure water by HTIC. (f) Degradation of SMX, SA and SD in lake water by HTIC.

In investigation of the degradation performance of HTIC, naphthalene (NAP), tetracycline (TC), and sodium diclofenac (DCF) were selected as target pollutants. Degradation experiments were conducted in both pure water and lake water. Notably, HTIC maintained high degradation efficiency towards NAP, TC, and DCF even after 60 minutes of continuous visible-light irradiation, with degradation rates exceeding 90% in pure water and remaining above 75% in lake water. These results indicate the universal adaptability of HTIC for pollutant removal. Furthermore, in the presence of natural organic matter (NOM) at varying concentrations, the degradation efficiency of HTIC was influenced, and this effect became more pronounced with increasing NOM concentration. Nevertheless, the degradation rate in pure water was consistently maintained above 85%, demonstrating HTIC's tolerance to interfering substances commonly present in water bodies. This also suggests that the structure of HTIC remains stable during the degradation process, underpinning its adaptability to complex environments and its sustained pollutant removal performance.

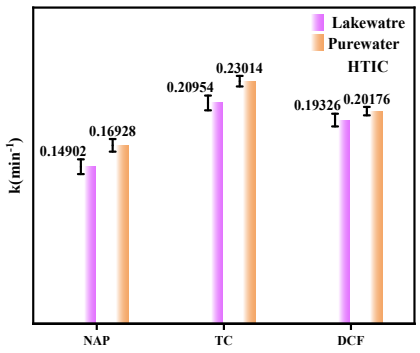

Figure S24 First-order degradation rate constant for photocatalysis of NAP, TC and DCF (5ppm) by HTIC in pure water and lake water.

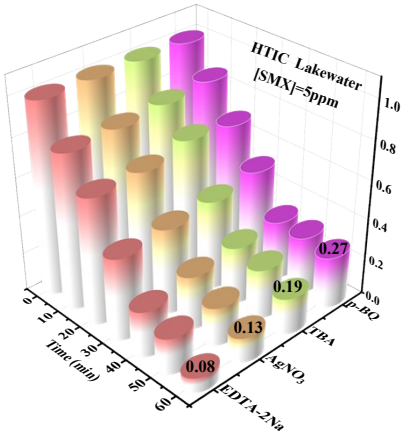

Figure S25 Degradation SMX in different sacrificial agents by HTIC. (f) Recycled degradation experiments by HTIC.

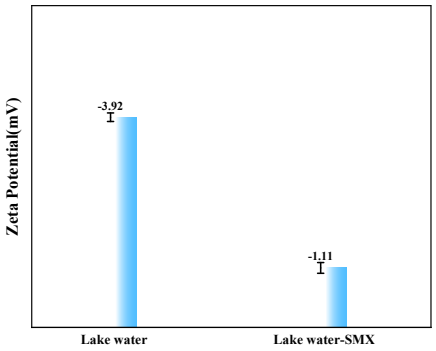

Figure S26. Zeta potential of HTIC in the (a) lake water; (b)lake water with SMX.

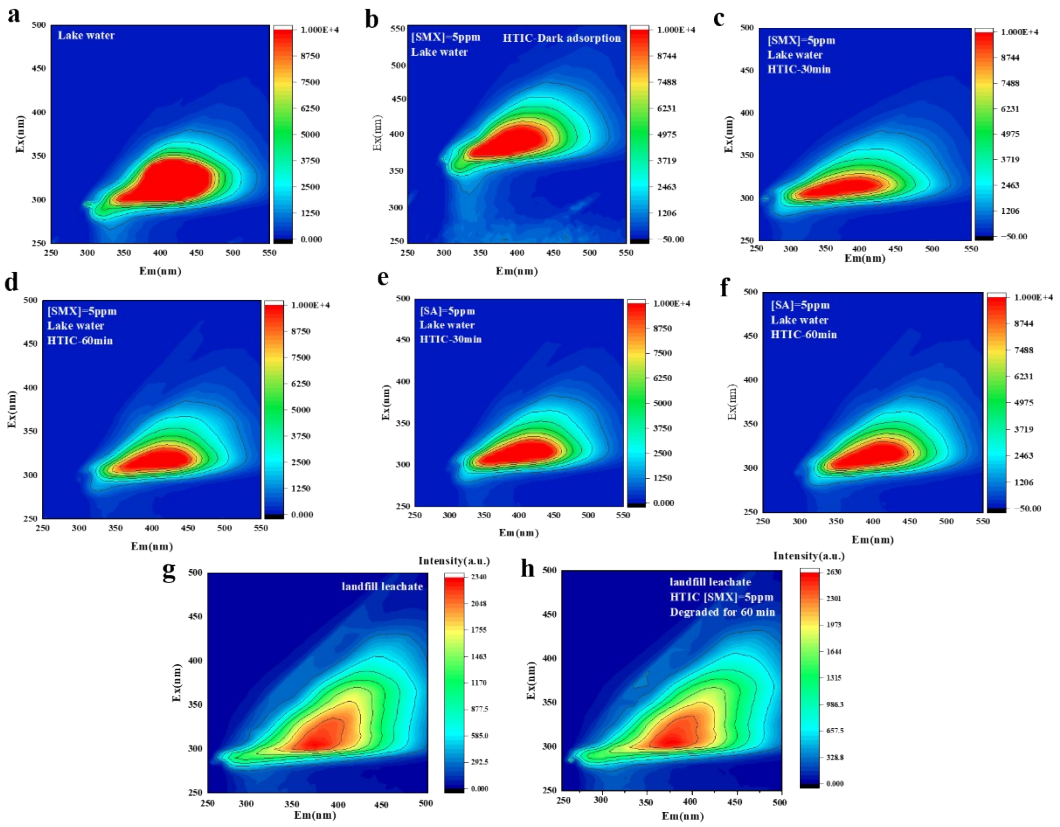

Figure S27. 3D EEM spectra during SMX and SA degradation process with HTIC in the lake water and landfill leachate.

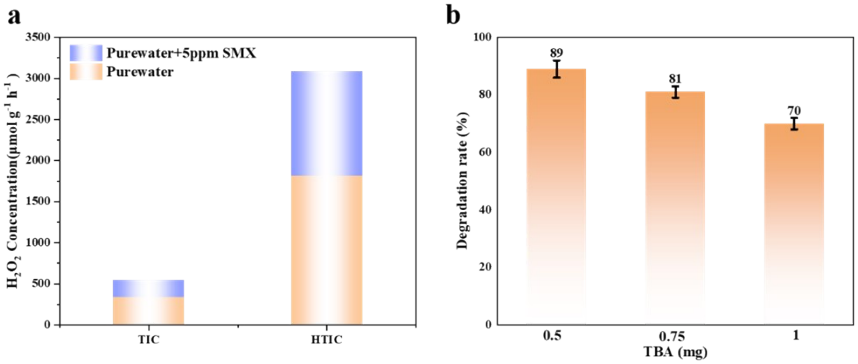

Figure S28. (a)Photocatalytic yield of H_2O_2 in pure water and pure water with SMX by TIC and HTIC. (b) The degradation rate of SMX at different concentrations of TBA by HTIC.

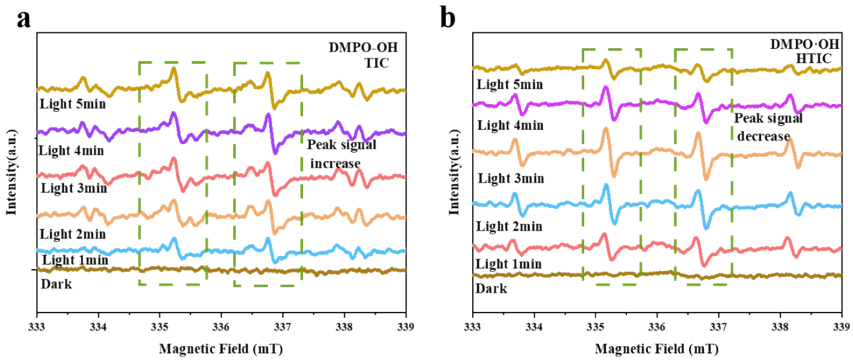

Figure S29. ESR spectra of ·OH.

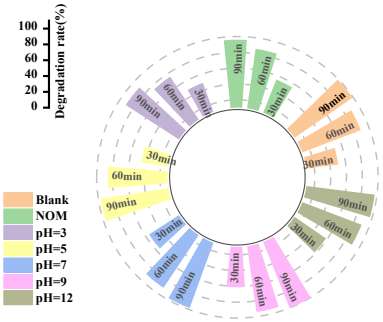

Figure S30 SMX removal efficiency by HTIC in different pH.

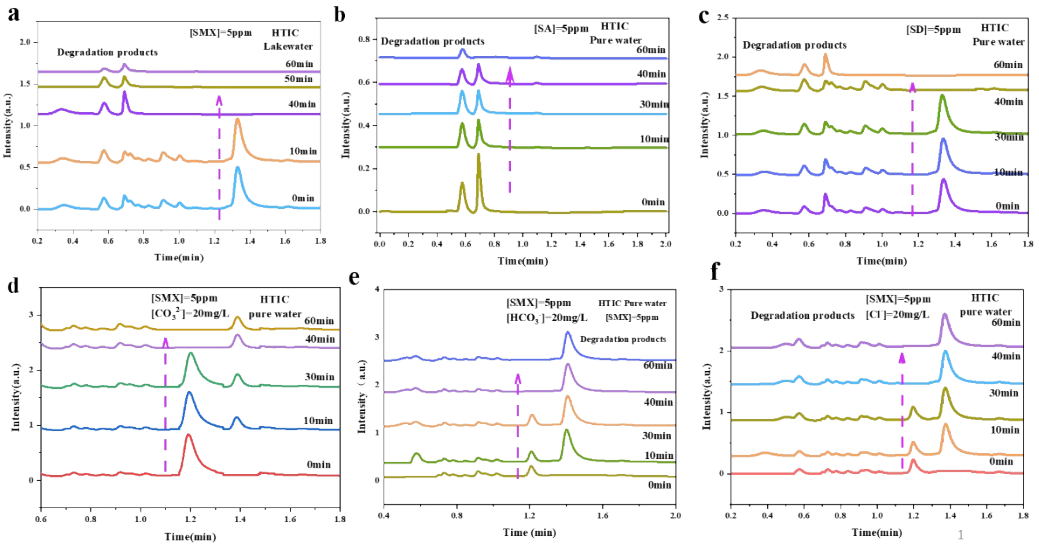

Figure S31. The UPLC chromatograms of the photocatalytic degradation by HTIC.

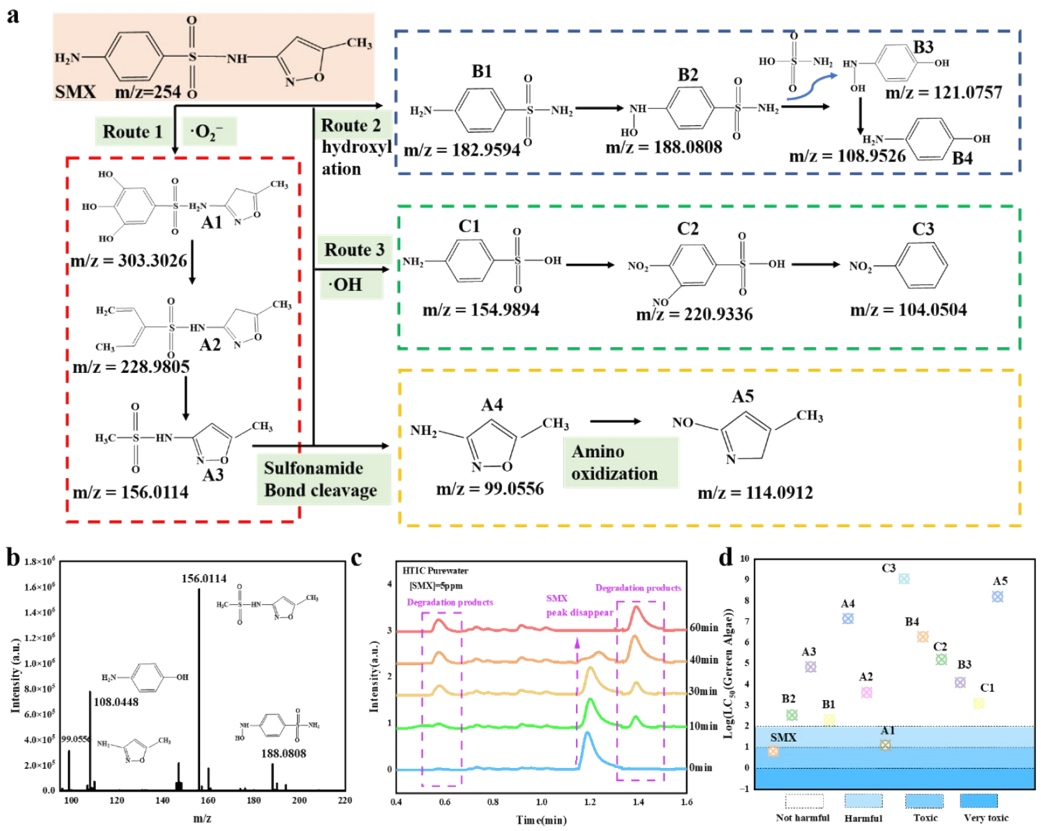

Figure S32 (a) Degradation pathways of SMX. (b)The LC-MS for SMX degradation by HTIC. (c) UPLC results of SMX degradation by HTIC in pure water. (d) Toxicity Assessment green algae by ECOSAR software.

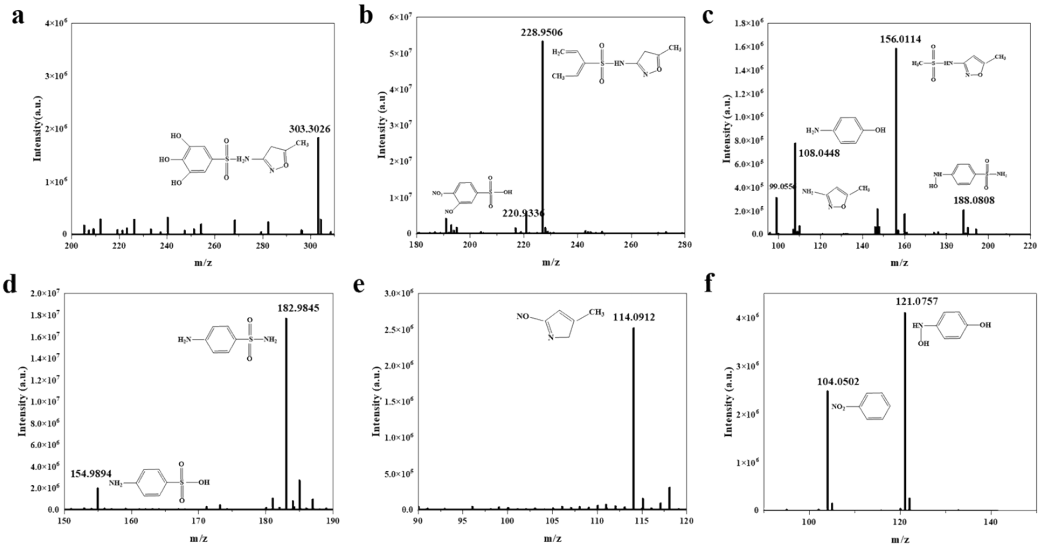

Figure S33. The LC-MS for SMX degradation products by HTIC.

In the photocatalytic degradation of SMX, the primary contributing reactive species are $\cdot O_2^-$ and ·OH. In Pathway A, $\cdot O_2^-$ attacks the benzene ring structure, inducing ring-opening reactions accompanied by the cleavage of the sulfanilamide bond and deamination,[19] ultimately mineralizing

into non-toxic small molecules. For Pathway B, ·OH possessing strong oxidative capability, preferentially attacks the electron-rich aniline amino group (-NH_2) on the SMX molecule, oxidizing it to a nitro group (-NO_2) and yielding nitro-SMX. As the degradation progresses, ·OH also randomly attacks multiple sites, generating various hydroxylated product isomers (e.g., para- and meta-hydroxylated SMX), and assaults the sulfonamide bond, leading to isoxazole ring cleavage. During hydroxylation (Pathway C), the introduction of -OH groups onto the SMX molecule significantly alters its polarity and water solubility, enhancing its reactivity and making it more susceptible to further oxidation. Overall, the photocatalytic degradation of SMX is a complex reaction process involving multiple reactive species, particularly ·OH and $\cdot O_2^-$. And ·OH predominantly drives the most potent oxidative reactions (e.g., amino group oxidation, benzene ring hydroxylation), while $\cdot O_2^-$ plays an indispensable role in cleaving heterocyclic structures. This process ultimately results in the complete degradation of SMX and its toxic intermediates into harmless inorganic substances, demonstrating the significant potential of photocatalytic technology in treating antibiotic contamination.

Table S7. Scope of Toxicity Assessment

Toxicity rang(mg/L)	Logarithmic-transformed toxicity rang	Class
$k \leq 1$	$\lg k \leq 0$	Very toxic
$1 < k \leq 10$	$0 < \lg k \leq 1$	Toxic
$10 < k \leq 100$	$1 < \lg k \leq 2$	Harmful
$k > 100$	$\lg k > 2$	Not harmful

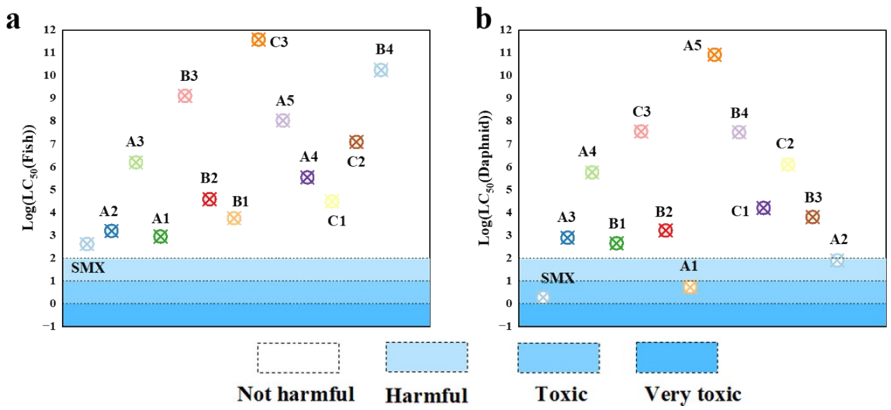

Figure S34 The toxicity assessment of SMX's degradation products (a) Fish, (b) Daphnia.

References

1 Becke, A.D, The Journal of chemical physics. 1996, **104**, 1040-1046.

2 Grimme S, Antony J, Ehrlich S, Krieg H, J. Chem. Phys. 2010, **132**, 154104.

3 Weigend, F, Ahlrichs, R. Phys. Chem. Chem. 2005, **7**, 3297–3305.

4 Tian Lu, Feiwu Chen, J. Comput. Chem. 2012, **33**, 580-592.

5 Humphrey, W., Dalke, A., & Schulten, K, Journal of Molecular Graphics. 1996, **14**, 33-38.

6 Z. Zhou, M. Sun, Y. Zhu, P. Li, Y. Zhang, M. Wang, Y. Shen, Applied Catalysis B: Environmental. 2023, **334**, 122862.

7 C. Wu, Z. Teng, C. Yang, F. Chen, H.B. Yang, L. Wang, H. Xu, B. Liu, G. Zheng, Q. Han, Advanced Materials. 2022, **34**.

8 R. Sun, X. Yang, X. Hu, Y. Guo, Y. Zhang, C. Shu, X. Yang, H. Gao, X. Wang, I. Hussain, B. Tan, Angewandte Chemie International Edition. 2024.

9 Y. Hou, P. Zhou, F. Liu, Y. Lu, H. Tan, Z. Li, M. Tong, J. Ni, Angewandte Chemie International Edition. 2024, **63**.

10 Y. Mou, X. Wu, C. Qin, J. Chen, Y. Zhao, L. Jiang, C. Zhang, X. Yuan, E. Huixiang Ang, H. Wang, Angew Chem Int Ed Engl. 2023, **62**, e202309480.

11 X. Bai, L. Guo, T. Jia, Z. Hu, Journal of Materials Chemistry A. 2024, 12, 13116-13126.

12 J.Y. Yue, J.X. Luo, Z.X. Pan, R.Z. Zhang, P. Yang, Q. Xu, B. Tang, Angewandte Chemie International Edition. 2024, **63**.

13 Y. Guo, Y. Dong, B. Liu, B. Ni, C. Pan, J. Zhang, H. Zhao, G. Wang, Y. Zhu, Advanced Functional Materials. 2024, **34**.

14 H. Li, Y. Li, X. Lv, C. Liu, N. Zhang, J. Zang, P. Yue, Y. Gao, C. Liu, Y. Li, Advanced Materials. 2025, **37**.

15 Cheng H, Lv H, Cheng J, Wang L, Wu X, Xu H, Advanced Materials. 2021, **34**.

16 W. Zhao, P. Yan, B. Li, M. Bahri, L. Liu, X. Zhou, R. Clowes, N. D. Browning, Y. Wu, J. W. Ward, A. I. Cooper, J Am Chem Soc. 2022, **144**, 9902-9909.

17 X. Luo, S. Zhou, S. Zhou, X. Zhou, J. Huang, Y. Liu, D. Wang, G. Liu, P. Gu, Advanced Functional Materials. 2024, **35**.

18 Y. Zhang, C. Pan, G. Bian, J. Xu, Y. Dong, Y. Zhang, Y. Lou, W. Liu, Y. Zhu, Nature Energy. 2023, **8**, 361-371.

19 K. Zhi, D. Liu, J. Xu, Z. Li, S. Li, L. Luo, G. Gong, R. Han, A. Yin, L. Guo, Chemical Engineering Journal. 2025, **512**.